2017

Design of a compact, fully-autonomous 433 MHz tunable antenna for wearable wireless sensor applications

John Buckley

Kevin McCarthy

Domenico Gaetano

See next page for additional authors

Authors
John Buckley, Kevin McCarthy, Domenico Gaetano, Loizos Loizou, Brendan O'Flynn, and Cian O'Mathuna

IET Microwaves, Antennas & Propagation

Research Article

Design of a compact, fully-autonomous 433 MHz tunable antenna for wearable wireless sensor applications

ISSN 1751-8725
Received on 1st March 2016
Revised 22nd September 2016
Accepted on 1st November 2016
E-First on 22nd December 2016
doi: 10.1049/iet-map.2015.0712
www.ietdl.org

John L. Buckley[1] ✉, Kevin G. McCarthy[2], Domenico Gaetano[3], Loizos Loizou[4], Brendan O'Flynn[1], Cian O'Mathuna[1]

[1]*Wireless Sensing Systems, Tyndall National Institute, Lee Maltings, Dyke Parade, Cork, Ireland*
[2]*School of Engineering, Electrical and Electronic Engineering, University College Cork, Cork, Ireland*
[3]*Antenna and High Frequency Research Centre, Dublin Institute of Technology, Dublin, Ireland*
[4]*Guinness Enterprise Centre, Benetel Ltd., Taylor's Lane, Dublin, Ireland*
✉ *E-mail: john.buckley@tyndall.ie*

Abstract: The authors present the design of a tunable 433 MHz antenna that is tailored for wearable wireless sensor applications. This study first presents a detailed analysis of the measured impedance characteristics of a chosen antenna under test (AUT) in varying proximity to a human test subject. Instead of limiting the analysis to the head and hand only, this analysis measures the AUT impedance at varying distances from 11 different body positions. A novel antenna equivalent circuit model is then developed that enables both the free-space and total on-body AUT impedance variation to be rapidly computed using a circuit simulator instead of the requirement for computationally intensive finite-element methods for example. The design and characterisation of a tunable matching network that enables AUT impedance matching for 11 different positions on the human body is then outlined. Finally, a fully-autonomous 433 MHz tunable antenna is demonstrated. The antenna occupies a small printed circuit board area of 51 × 28 mm and is printed on standard FR-4 material with the tuner completely integrated into the antenna itself. Prototype measurements show an improvement of 3.9 dB in power delivery to the antenna for a load voltage standing wave ratio of 17:1, with a maximum matching loss of 0.84 dB and S_{11} (−10 dB) ≥ 18 MHz for all load conditions.

1 Introduction

The development of wireless sensor networks (WSNs) using wearable devices is seeing a rapid emergence in recent times, specifically in areas such as healthcare and fitness monitoring [1, 2]. In addition, the emerging paradigm of the Internet of Things is enabling a wide variety of increasingly inexpensive wireless sensors for personal smart-health systems [3]. These types of WSN applications, often referred to as body sensor networks (BSNs), require highly integrated wireless sensor devices that can be used in a wearable configuration, to wirelessly monitor various physiological parameters of the user. The 2.45 GHz frequency band is currently a popular choice for these devices. However, other frequency bands such as the 433 MHz industrial scientific and medical (ISM) band can offer certain advantages as less repeaters are required and band congestion in the 2.45 GHz bands is a growing issue [4, 5]. Widespread adoption of wearable wireless technology is being driven by continued integration that allows small sized devices to be conveniently placed on different parts of the body. Small sized antennas are therefore a key requirement, but it is well known that electrically small antennas are prone to impedance and resonant frequency variation due to human body effects [6] as well as radiation pattern degradation [7].

At the present time, WSN research platforms [8–11] use fixed antenna impedance matching networks that cannot adapt to changing antenna environments such as in wearable BSN applications. Adaptive antenna tuning networks are extremely desirable and have been investigated by many researchers in recent times for cellular applications [12, 13]. These antenna tuning solutions offer potential benefits for cellular applications where human hand and head effects are of key concern. However, little is reported in the literature in relation to the development of antenna tuning solutions for the emerging field of wearable WSN applications where the antenna can be placed at a wide variety of positions across the entire human body.

In this work, the investigation is strongly focused on measurement and circuit modelling methods to analyse dynamic antenna impedance changes due to human body effects. In addition, we present the design of a fully autonomous, 433 MHz tunable antenna solution that can automatically adapt to changing antenna impedances in wearable wireless sensor applications. Antenna performance parameters other than impedance, such as gain, efficiency, current density and radiation patterns are also affected by the presence of the human body [7, 14–18]. The effects of the human body and matching network on these performance parameters are beyond the scope of this work, but is the subject of future work. The initial architecture for a larger, custom antenna return loss measurement and tuning system was developed and described in detail in [19, 20]. The described system is substantially miniaturised compared with the previous system and is now integrated onto the antenna substrate itself, leading to a lower-loss, lower-power implementation. A brief outline of this paper is summarised as follows. Section 2 presents a measurement technique to determine the total impedance variation of a chosen antenna under test (AUT) when placed at several locations on the human body. Section 3 presents an equivalent circuit model of the AUT that also includes human body effects. Sections 4 and 5 discuss the design and characterisation of the tunable antenna and Section 6 concludes the paper.

2 Antenna impedance variation on the human body

The first goal of this work was to determine the total antenna impedance variation of a chosen AUT when placed in varying proximity to different parts of a human test subject. A photograph of the AUT is shown in Fig. 1*a*. This is a compact, low-cost 433 MHz antenna structure that was designed for WSN applications and is described in detail in [21]. The antenna has dimensions of 51 × 28 mm with a substrate height of 1.53 mm and a copper thickness of 0.035 mm. The input impedance of the AUT is

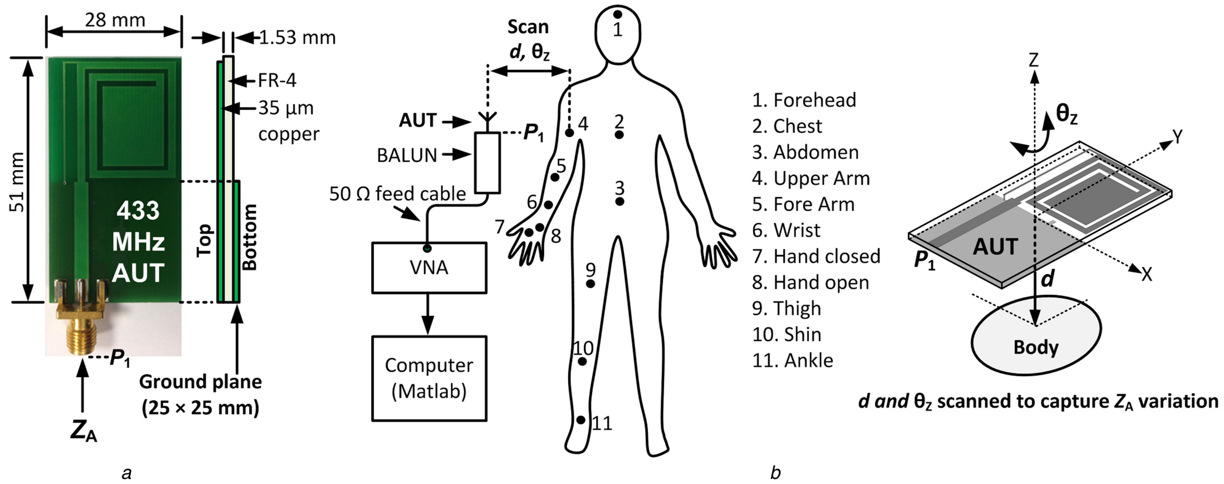

Fig. 1 *Details of AUT and on-body antenna measurement setup using a human test subject*
(a) Photograph of 433 MHz AUT, ***(b)*** Overview of measurement setup for on-body AUT characterisation

denoted Z_A and is measured at $f_0 = 433$ MHz. The antenna measurement setup is shown in Fig. 1*b* with the AUT connected to a Rohde & Schwarz ZVRE [22] vector network analyser (VNA) via a 50 Ω cable and balun [23] to suppress unwanted feed cable radiation during measurements. The AUT was then placed at one of 11 different body locations shown with the human test subject clothed and in a standing position. In this case, the antenna-body distance d was then scanned repeatedly from a maximum distance d_{MAX} of 6 cm approximately (representing the distance beyond which the AUT impedance does not change) to a minimum distance $d_{MIN} = 1$ mm. The minimum distance d_{MIN} was set using a 1 mm foam spacer attached to the bottom side of the antenna to prevent human skin contact whose high conductivity would effectively create a short circuit at the antenna terminals when placed at the forehead, hand and wrist locations in Fig. 1*b*. The *x–y* plane of the antenna was kept approximately parallel to the surface of the skin during these measurements.

In addition to repeatedly moving the AUT uni-laterally along the *z*-axis, the antenna was also rotated about the *z*-axis by an angle denoted θ_Z in the range $0° \leq \theta_Z \leq 360°$ in order to capture any impedance variation due to orientation in this configuration. A computer running a Matlab [24] script was used to continuously measure and record all values of S_{11} at Port P_1. Each of the measurements was performed for a 90 s period, resulting in a total of approximately 750 discrete measurements per body position for all variations of distance d and angle θ_Z. The AUT measurements for 11 different body positions are shown in Fig. 2. The upper and lower body responses of Figs. 2*a* and *b* show that different body locations produce different impedance responses and it is therefore necessary to consider the effects of the entire human body to determine the total AUT impedance variation. The measured effects of pocket objects such as a wallet, coin, car keys and IPhone 5 are shown in Fig. 2*c*. Conductive metal objects such as the coin, lead to highest measured voltage standing wave ratio (VSWR) values, with the measured AUT impedance moving to the extreme right-hand side of the Smith chart. Fig. 2*d* shows the superposition of all measured data on the same graph, denoted Z_{A_TOT}. This impedance data represents the total AUT impedance variation that was measured for all distances d and θ_Z across 11 body positions. The measured data shows that the AUT impedance behaves in a predictable manner with both the inductive and resistive components of Z_A increasing with decreasing values of d. In order to better understand the observed AUT behaviour in varying proximity to the human body, a transmission line antenna model is next investigated.

3 Antenna transmission line model with human body-loading effects included

Equivalent transmission line models for IFA antennas in free-space have been reported previously in the literature [23, 25]. In this work, the motivation was to present a transmission line antenna model of the 433 MHz AUT that also accounts for human body effects on the input impedance of the antenna. A simplified schematic representation of the antenna is shown in Fig. 3*a* and shows the SMA input at Port P_1 and microstrip line with all the other antenna elements labelled from Point *A* to Point *D*.

An equivalent circuit for the antenna was then developed using AWR Microwave Office [26] as shown in Fig. 3*b*. The antenna feed at Port P_1 is connected to a 50 Ω coaxial transmission line T_{SMA} representing the on-board SMA connector with characteristic impedance $Z_{0\ SMA} = 50\ \Omega$ and electrical length $\Theta_{SMA} = 3°$ at 433 MHz. T_{SMA} is connected to a 50 Ω microstrip line T_0 of width $W_0 = 2.91$ mm and physical length $Len_0 = 25$ mm.

The shunt inductive loop comprising segments Seg_1 and Seg_2 were modelled as a series combination of inductors L_1 and L_2. Spiral arms Seg_3 and Seg_4 were modelled as two transmission lines T_1 and T_2 with characteristic impedances Z_{01} and Z_{02} and electrical lengths Θ_1 and Θ_2 respectively. Series resistances R_1 and R_2 were used to model the distributed radiation and loss resistances associated with Seg_3 and Seg_4. Lumped capacitance C_1 was used to account for the capacitive stub at Point *C*. Finally, the end-capacitance of the patch at Point *D* was modelled as a lumped capacitance C_2 to ground. The equivalent circuit model parameters, except those for the SMA connector and microstrip line, were then optimised against measured one-port AUT S-parameter data over the range 400–500 MHz using AWR Microwave Office and the final optimised parameters are listed in Table 1.

The optimised parameters show that the total electrical length of the spiral sections ($\Theta_2 + \Theta_3$) is 85° approximately. This value is slightly less than a resonant $\lambda_0/4$ length of 90° at f_0, but is expected since the capacitive end-loading due to C_2 accounts for a small decrease in resonant length and is consistent with the findings of [25]. Figs. 4*a* and *b* compare the S_{11} responses of the measured AUT and equivalent circuit and very good correlation is observed for the magnitude and phase of S_{11} across a 100 MHz frequency range. Incorporation of human body loading effects in the equivalent circuit model was also investigated to help explain the previously measured antenna impedance variation in proximity to the human body. Since the patch element and ground-plane have the largest cross-sectional-area, when compared to the other antenna features, it was first assumed that the majority of the capacitive coupling between the antenna and human body occurs via patch capacitance C_P and ground capacitance C_G as illustrated in Fig. 4*c* with both C_P and C_G assumed to decrease with increasing antenna-body distance d. In addition to the above, it was also assumed that the human body has a variable conductance G_B,

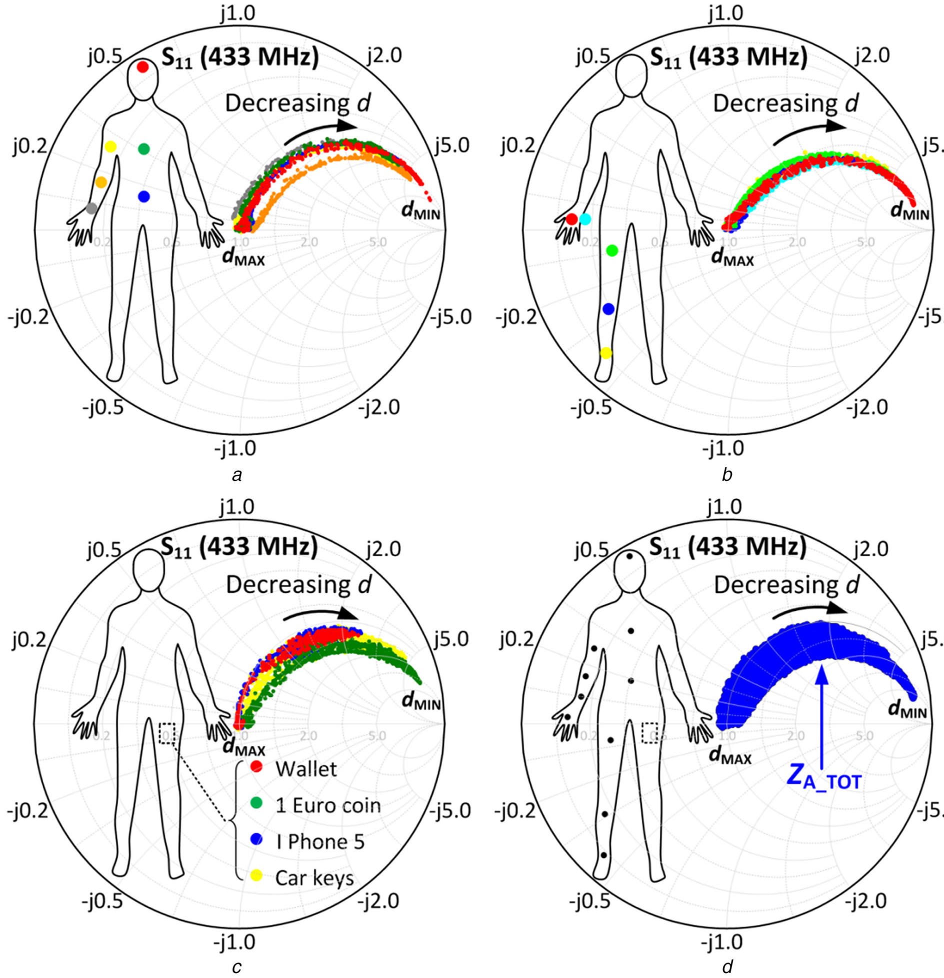

Fig. 2 *Summary of on-body AUT impedance measurements*
(a) Upper body, ***(b)*** Lower body, ***(c)*** Pocket Items, ***(d)*** Superposition of all measurements (Z_{A_TOT})

depending on the characteristics of the body tissue above which the antenna is positioned.

The series equivalent of C_P, C_G and G_B was then modelled as a simple parallel equivalent of C_3 and R_3 that was added to the earlier equivalent circuit of Fig. 3*b* at point *D*. The range of parameters C_3 and R_3 were then determined experimentally in simulation, with C_3 varied from 0 to 0.2 pF in steps of 2 fF and R_3 varied from 29.5 to 309.5 kΩ in steps of 20 kΩ. Fig. 4*d* compares the simulated values of S_{11} using the equivalent circuit model versus measurements on the AUT. Quantity Z_{A_TOT} denotes the total measured impedance variation of the AUT for 11 body positions or approximately $11 \times 750 = 8250$ individual measurements. Fig. 4*d* shows that the simulation model is capable of providing a good estimate of the measured Z_{A_TOT} values. Accounting for human body antenna loading effects using an equivalent circuit model, rather than using EM methods has particular benefits in terms of computation time. For example, in related work that is not discussed here, a finite-element-method (FEM) model was developed with the AUT placed at the wrist position (similar to the configuration of Fig. 1*b*) at varying distance *d* above a phantom human arm. This model required approximately 1.5 h to compute Z_{ANT} for eight discrete values of *d*, using a PC with 24 GB of RAM and an Intel® Xeon® 8-core CPU running at 1.6 GHz. In contrast, the equivalent circuit model allows a total of 1515 discrete S_{11} antenna values to be computed in a time of 0.54 s or 1.9×10^6 times faster. The proposed equivalent circuit is not intended to replace EM modelling methods, but has the advantage of enabling a fast analysis to be performed while also providing insight into the detuning behaviour of the AUT in proximity to the human body.

4 Antenna tuner design

In the previous section, the total impedance variation of the AUT for 11 body positions was measured. In this section, this data is used in the design of a tunable antenna that adaptively corrects for antenna impedance mismatch. To determine the potential benefits of impedance matching, the losses due to impedance mismatch are first evaluated when no matching network is present. This is achieved by determining the antenna mismatch loss (*ML*) or amount of power that is lost from the generator due to impedance mismatch at the input terminals of the antenna [27] and is defined as follows:

$$ML(\mathrm{dB}) = -10\log_{10}\left(1 - |S_{11}|^2\right), \tag{1}$$

where S_{11} is the antenna reflection coefficient [28]. Fig. 5 shows the previously measured values of Z_{A_TOT} superimposed on the calculated contours of *ML* using (1) for varying S_{11} at 433 MHz with a source impedance $Z_S = Z_0 = 50\ \Omega$. A significant, worst-case *ML* of approximately 6 dB is observed without matching for this AUT.

To reduce the above losses due to impedance mismatch, the following presents the design of a reconfigurable impedance matching network. The main requirements for the matching network are that it provides the required impedance coverage to match all possible antenna load impedances Z_{A_TOT}, with minimal loss over a specified bandwidth of approximately 2 MHz for the 433 MHz ISM-band. Several different types of low-pass topologies were investigated including *L*, double-*L*, *T* and Π-type networks. The main disadvantages of the *L*-network are limited loaded quality factor and bandwidth. In addition, conjugate matching is possible only for a limited area of the Smith chart [29], even when

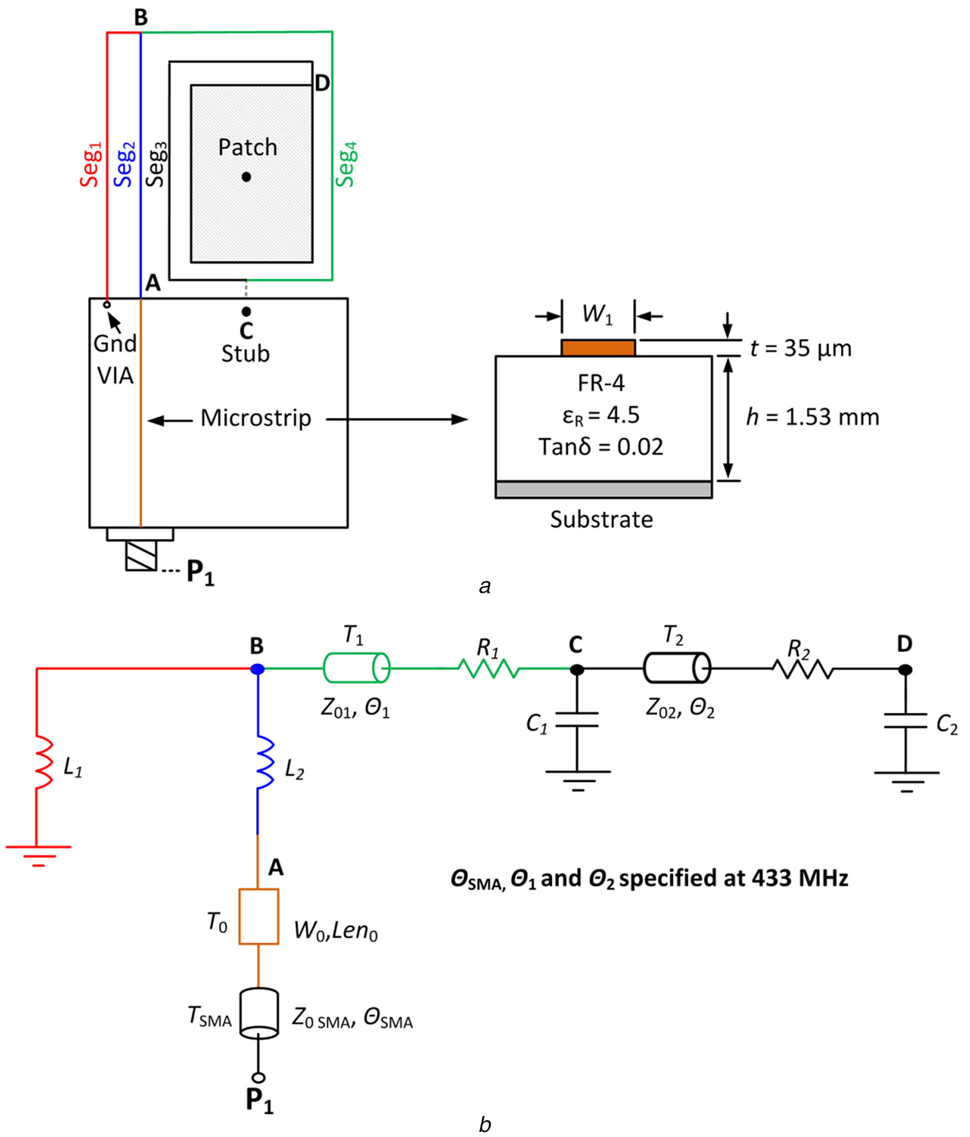

Fig. 3 *Transmission line model of 433 MHz AUT*
(a) Simplified schematic representation, ***(b)*** Equivalent circuit model

ideal, lossless components are used. The double-L, low-pass network can offer increased coverage and bandwidth, but has the disadvantage of requiring an extra series inductor which leads to increased losses. The low-pass T-network has only one tunable component and therefore has limited impedance coverage. The Π-structure was eventually chosen for this application as this topology minimises the effect of finite-Q-factor tunable and fixed components that are used to implement the network and also provides the necessary Smith chart coverage.

A simplified representation of the Π-type matching network is shown in Fig. 6*a*. Reconfigurability is achieved using variable capacitances C_1 and C_2 using a commercial PE64102 device [30]. This is a 5-bit device that allows the capacitance between the RF+ and RF− terminals to be tuned from $C_{\text{MIN}} = 1.88$ pF to $C_{\text{MAX}} =$ 14.0 pF in 32, discrete steps of 391 fF. In terms of accurately predicting the performance of the matching network, the component parasitics of C_1 and C_2 are essential to model and an equivalent circuit model of the component was therefore employed [30]. Similarly, the quality-factor Q_{L1} of the fixed inductor was used to model the inductor losses, specified at f_0. The use of a high Q-factor inductor is essential to minimise losses and an air-core type was chosen with $Q_{\text{L1}} = 110$ [31].

Fixed capacitor C_3 was used to provide additional capacitance at the source side of the matching network to enable high VSWR load impedances to be matched. A bi-directional coupler C_{OUP1} [32] was employed at the output of the matching network to monitor the levels of forward and reflected power at the antenna terminals and the chosen coupler [32] was selected to have minimal insertion loss (0.25 dB at 433 MHz). When a two-port matching network is connected between a source and variable load impedance, it is necessary to consider the losses of the matching network and the effect of reflections at the source and load as defined by the two-port transducer power gain G_{T} [28]. A load-pull analysis and optimisation of the simulation model was then performed using Agilent's Advance Design System (ADS) [33] to optimise L_1 and C_3 for maximum G_{T} over the range of antenna impedances defined by $Z_{\text{A\_TOT}}$ and the resulting G_{T} contours are shown in Fig. 6*b*. It can be seen that the Π-Type matching network provides good impedance coverage with significant improvement

Table 1 Final optimised equivalent circuit model parameters

Parameter	Value	Parameter	Value
R_1	9.57 Ω	$Z_{0\text{SMA}}$	50 Ω
R_2	11.1 Ω	θ_{SMA}	3°
C_1	0.14 pF	Z_{01}	166.2 Ω
C_2	0.31 pF	Θ_1	55.08°
L_1	10.48 nH	Z_{02}	443.4 Ω
L_2	29.23 nH	Θ_2	30.13°

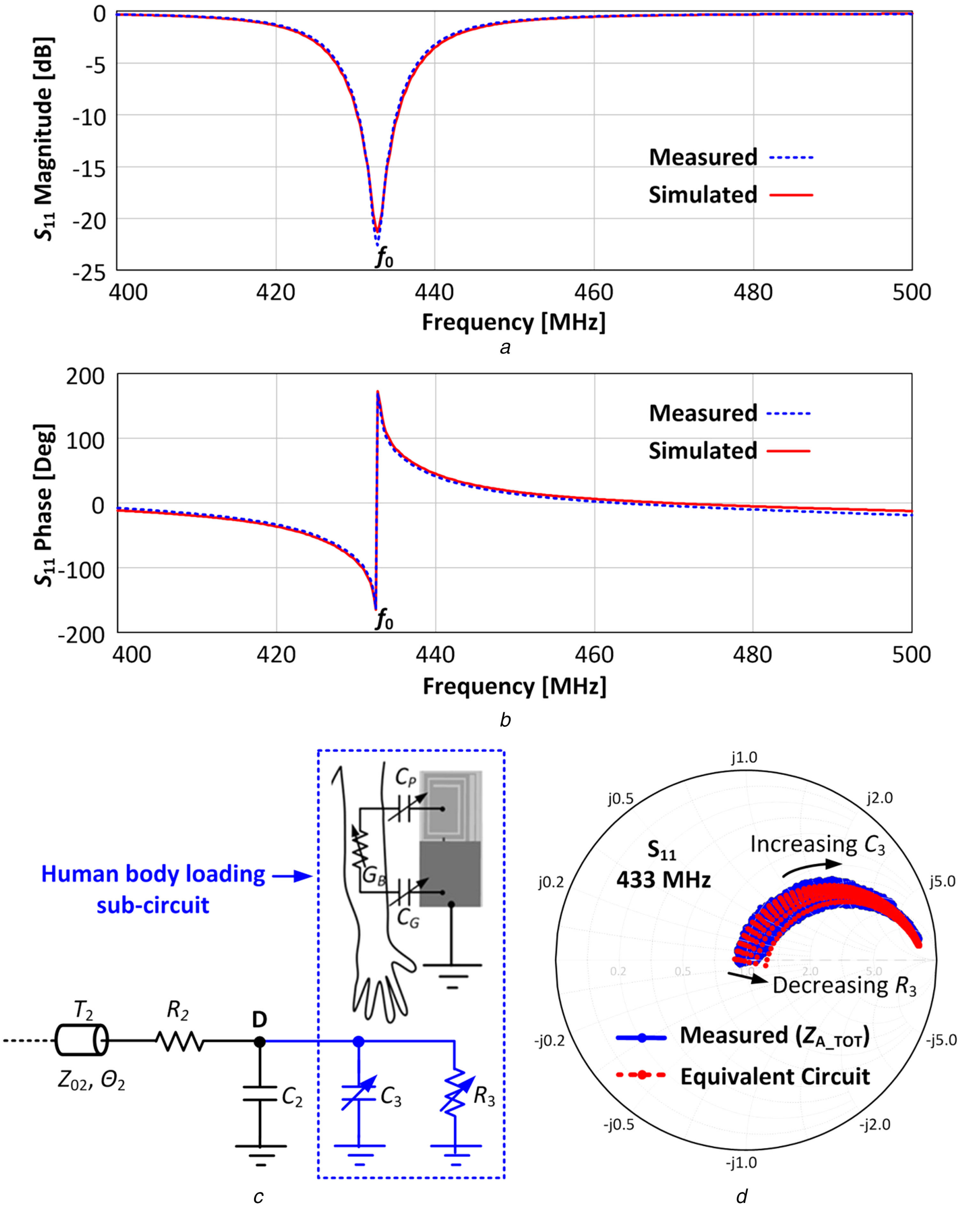

Fig. 4 *AUT equivalent circuit model*

(a) Comparing measured and simulated S_{11} magnitude (400–500 MHz), ***(b)*** Comparing measured and simulated S_{11} phase (400–500 MHz), ***(c)*** Addition of human body loading sub-circuit (blue) to previous antenna equivalent circuit of Fig. 3*b*, ***(d)*** Comparing measured and simulated total on-body S_{11} responses at 433 MHz

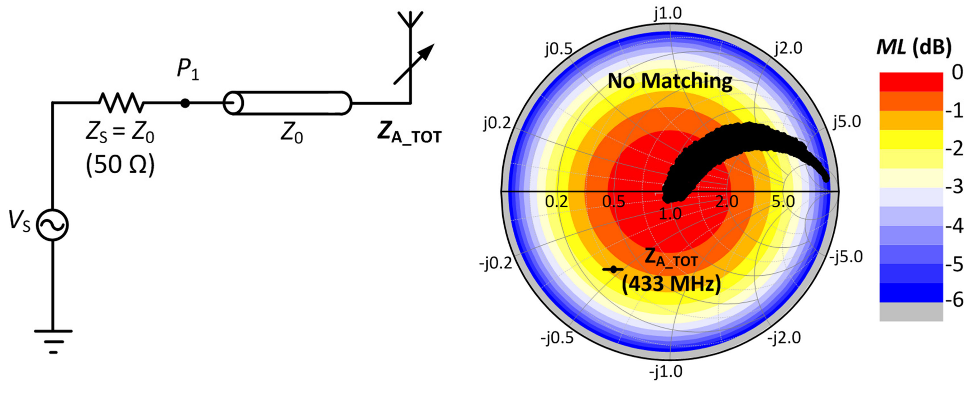

Fig. 5 *Simulated AUT ML with no matching network present*

in power delivery to the antenna for high antenna VSWR when compared with the unmatched case.

For example, as outlined previously, the worst-case AUT *ML* loss was 6 dB without matching. With matching, the simulated loss is approximately 3 dB maximum, or a 3 dB improvement in power delivery to the antenna. For values of Z_{ANT} near the centre of the Smith chart, the simulation model predicts maximum losses of approximately 0.8 dB, mainly attributed to losses in components C_1, C_2, L_1 and C_{OUP1}.

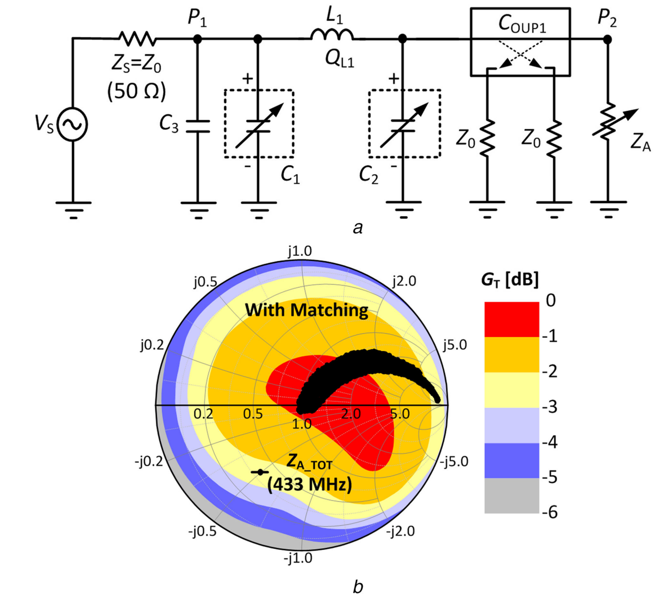

Fig. 6 *Π-type matching network*
(a) Simplified representation of the Π-type matching network, ***(b)*** Simulated optimised G_T contours

5 Antenna tuner implementation and measured results

In this section, the hardware implementation details of a small-footprint, 433 MHz antenna with integrated tuner are presented. The initial architecture was described in detail in [19, 20]. Here, a similar but more optimised, integrated and low power, discrete component solution is presented. A dedicated antenna tuner module was first developed for characterisation purposes and a block diagram is shown in Fig. 7*a* with a photograph of the fabricated module shown in Fig. 7*b*. Port P_1 of the matching network is the interface to the radio transceiver and Port P_2 is the antenna interface. Coupler C_{OUP1} allows the magnitude of the reflection coefficient $|\Gamma_L|$, at the antenna port to be measured and the chosen device has a coupling factor of 20 dB with a directivity of 30 dB to enable accurate measurement of $|\Gamma_L|$ as described in [19]. Instead of using two separate RF power detectors as in [19], in this case, a simpler and lower power alternative is employed using a single power detector with an RF switch SW_1 [34] used to select either of the P_{FWD} or P_{REF} signals. A LT5538 RF power detector [35] was chosen as this is a high sensitivity device with a dynamic range from −75 to +10 dBm and provides the required RF sensitivity for accurate measurement of antenna return loss. The power detector output is filtered and digitised by a low-power, ATmega128L micro-controller [36] and a pre-calibrated look-up table is used in firmware to compute the final values for P_{FWD} and P_{REF}. An RS-232 interface is also available for real-time monitoring of antenna measurement data via a graphical user interface. The tuner uses standard, 1.6 mm FR-4 material ($\varepsilon_R = 4.5$, $\tan\delta = 0.02$), with a six-layer stackup and is integrated in a small area of 25 × 28 mm. The tuning circuitry was placed on the top layer of the PCB with the tuning controller placed on the bottom layer. The DC supply is applied via the JTAG connector.

During characterisation, a one-Port S-parameter measurement was conducted using a Rohde & Schwarz ZVRE VNA [22] that was connected to P_2. Fig. 7*c* compares the measured and simulated values of S_{22}^{*} or the range of antenna impedances that can be conjugately matched to a 50 Ω impedance at the antenna port P_2 with the input port of the network P_1 terminated in 50 Ω (via the internal termination of the VNA). It can be observed that the tuner provides a good level of impedance coverage at port P_2 with strong agreement shown between simulation and measurement.

To compare the performance with and without the matching network present, the relative transducer gain ΔG_T was then measured [13], using a manual, two-port load-pull setup with a ZVRE VNA and Maury Model 1878G, triple stub tuner [37] to adjust the load VSWR at P_2. The measured and simulated results are shown in Fig. 7*d*. It can be seen that the tuner provides increased power delivery to P_2 for a large span of VSWR values ranging from 2.4:1 to 17:1, with an improvement of 3.9 dB measured for worst-case VSWR at P_2. For load VSWR ≤ 2.4:1, the maximum tuner loss was measured at 0.84 dB.

The final tunable antenna is shown in Fig. 8*a* and incorporates both the tuner and antenna in a single design. The antenna uses identical PCB stackup and materials as the tuner module of Fig. 7*b*. The antenna measures 51 × 28 × 8 mm with the matching circuit placed on the top side and the tuning controller placed on the opposite side as shown. Fig. 8*b* shows the measured values of S_{11} for the AUT from 300 to 500 MHz with *no tuning* when the antenna is placed in free-space (ideal case), and on the human head and wrist. For the head and wrist test cases, the antenna was placed at a distance of approximately 1 mm above the skin surface using a LDPE spacer [38] to prevent skin contact. It can be seen that the AUT is correctly tuned for the free-space case, but significant detuning is observed when the AUT is placed close to the human body.

In contrast, Fig. 8*c* shows that the tunable antenna can be matched for all three cases with a measured −10 dB bandwidth of greater than 18 MHz. It can also be observed from Fig. 8*c* that two resonances are observed in the measured S_{11} responses. For example, in the free-space case, the addition of the matching network results in two resonances at frequencies of $f_1 = 403$ MHz and $f_2 = 430$ MHz approximately. This behaviour can be explained by comparing the measured S_{11} responses of the AUT and tunable antenna as shown in the Smith chart of Fig. 8*d* where the frequency is swept from 300 to 500 MHz. For the case of the AUT, the response shows a single resonance at 433 MHz lying inside the 2:1 VSWR corresponding to a measured antenna S_{11} of −9.5 dB. However, for the tunable antenna case, the addition of matching components C_1, C_2, C_3 and L_1 leads to a frequency response with an additional loop inside the 2:1 VSWR circle, leading to a well matched response and wider matching bandwidth when compared with the non-matched AUT case.

The tuning algorithm was implemented using a sequential search of the 1024 possible tuner states, taking approximately 370 ms to execute. Once the search is complete, the algorithm sets the final tuner state for maximum P_{FWD}. Current consumption measurements of the prototype tunable antenna show that it requires a peak supply current of 32 mA DC during a tuning operation. Once tuning is completed, the tuning controller is placed in standby mode and the RF power detector is placed in shut-down mode. In this mode, all current capacitor states for C_1 and C_2 are maintained, thereby maintaining the current impedance match settings. This mode also means that the DC supply current to the antenna can be significantly reduced to a value of approximately 0.25 mA. The micro-controller clock frequency used for the above measurements was 8 MHz.

In the case where the antenna is placed in a wearable device that is securely attached to the body during use with little movement possible, the tuning operation would need to be exercised once, after placement, with only periodic tuning required thereafter. In such cases, there is a clear benefit in terms of improving RF link quality and reducing power consumption, especially for battery-operated devices with limited capacity. Alternatively, in cases where there is a larger degree of human body movement, the antenna return loss can be measured more regularly to determine if the matching network needs to be re-tuned. In such cases, the power demand increases in direct proportion to the sampling rate required for the particular application.

As summarised in Table 2, the vast majority of antenna tuning solutions reported in the literature focus on cellular applications, whereas this work concentrates on analysis of antenna tuning solutions for wearable WSN applications. The literature generally focuses on the AUT placement for the head and hand cases only,

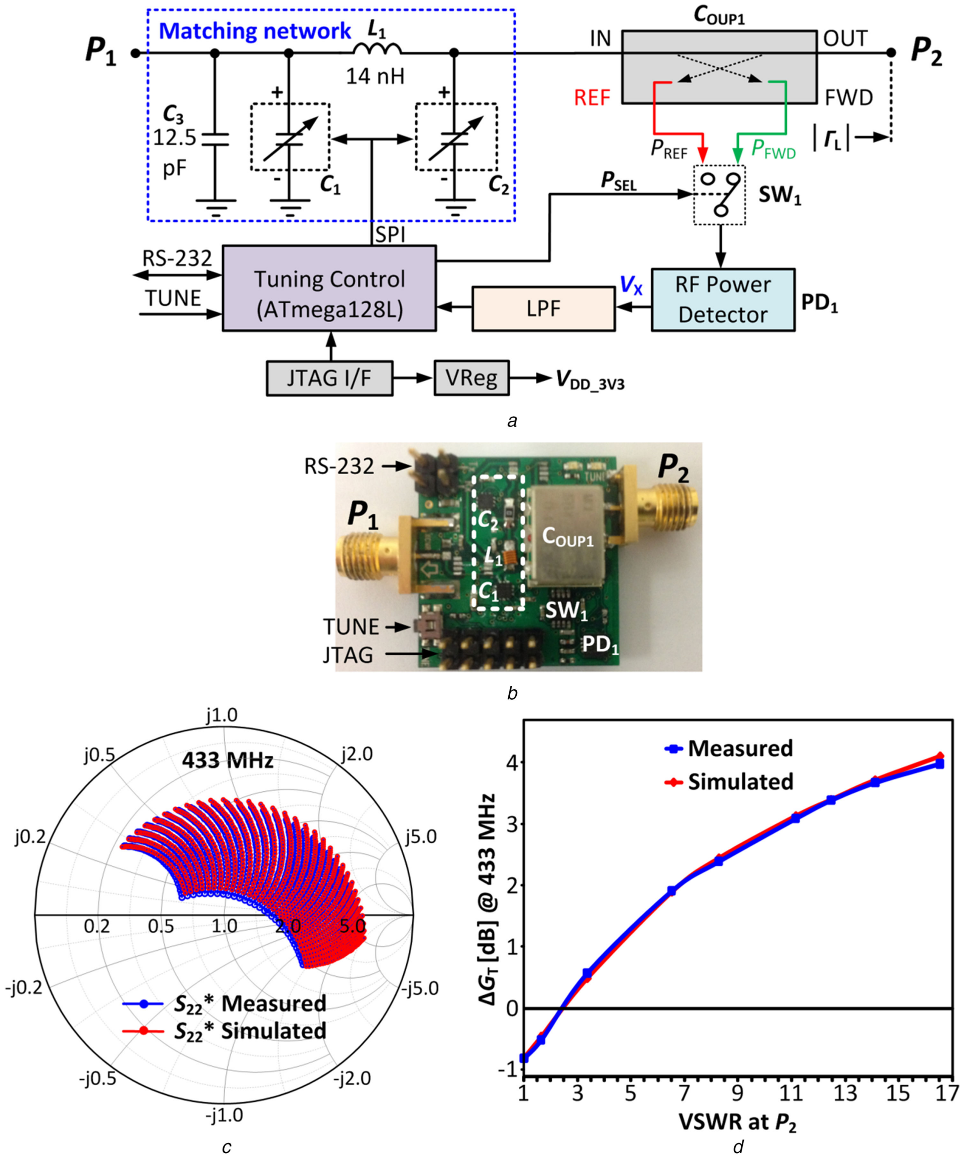

Fig. 7 *Details of antenna tuner module and measured performance*

(a) Block diagram of tuner module, ***(b)*** Photograph of tuner module, ***(c)*** Measured and simulated values of S_{22}^* at 433 MHz, ***(d)*** Comparing measured and simulated values of ΔG_T at 433 MHz

whereas this work considers AUT placement for a large number of different body positions as illustrated in Fig. 2 with eight antenna-body distances analysed for each body position. As explained in Section 1, a primary goal of this work is to explore the benefits of using the 433 MHz ISM band as an alternative to the 2.45 GHz ISM band that is most commonly used. When the tuner losses are compared, it can be seen that the developed antenna has losses in line with the majority of other works reported. However, use of the latest generation of low-loss silicon on insulator (SOI) tunable capacitor technology [41] will lead to reduced losses without any need to modify the design. Uniquely, the tunable antenna developed in this work does not require any supporting tuning hardware or external antenna as the tuner is integrated into the antenna element itself and capable of tuning autonomously.

6 Conclusions

This paper has presented the design of a tunable 433 MHz antenna that is tailored for wearable wireless sensor applications. It was shown that for a wearable wireless device to operate effectively across several body locations, it is essential to characterise the antenna across the entire human body rather that at a single location and a single distance from the body. An equivalent circuit antenna model was presented that includes human body effects, enabling rapid simulation of total antenna impedance variation when compared with FEM simulation methods. The design of an adaptive impedance matching network was then presented that allows AUT tuning across all 11 different body positions considered. Finally, a compact, 433 MHz tunable antenna was demonstrated. Prototype measurements show up to 3.9 dB improvement in power delivery to the antenna for a VSWR of 17:1 with a maximum loss of 0.84 dB and a −10 dB return loss bandwidth of ≥18 MHz. The proposed solution offers particular performance advantages for wearable wireless sensor systems in terms of improving power delivery to the antenna, reducing current consumption and providing longer battery life. Improved RF link quality and the need for less number of data re-transmissions is also a critical advantage for health-related applications. The prototype tunable antenna was developed as a stand-alone device, but could also be integrated into existing wearable systems. Although the work focuses on the 433 MHz ISM band, the same methods can be applied to other frequency bands. Future work will study the radiation characteristics of the antenna in close proximity to the human body as well as the effects of the matching network on these characteristics.

7 Acknowledgments

This work was supported by the EC SMArt Systems Co-design project (SMAC) FP7-ICT-2011-7-288827 and Enterprise Ireland

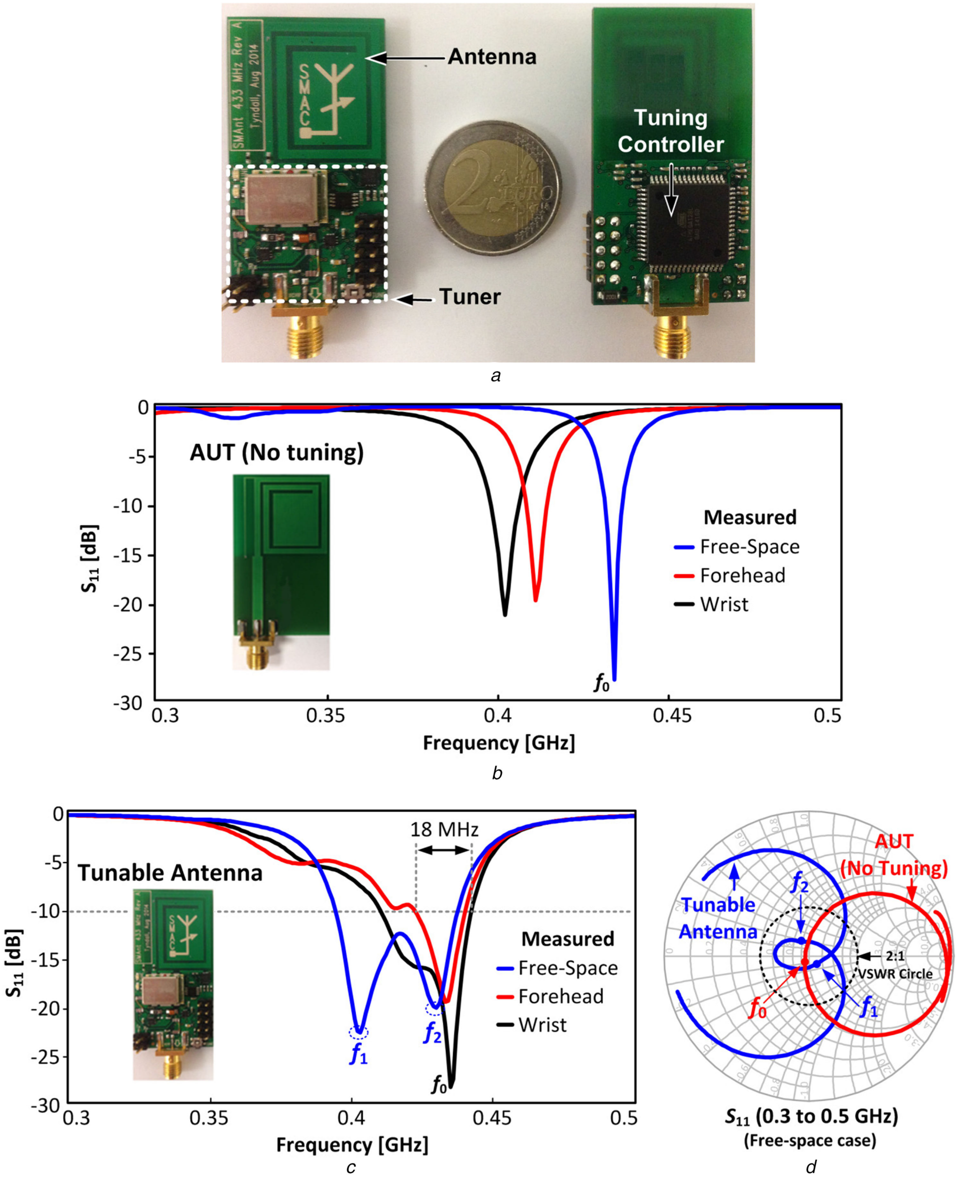

Fig. 8 *Final tunable antenna*

(a) Photograph showing top and bottom sides of tunable antenna, ***(b)*** Measured S_{11} return loss of AUT with no tuning, ***(c)*** Measured S_{11} of tunable antenna, ***(d)*** Comparing measured S_{11} of AUT and tunable antenna

Table 2 Comparison of this work to other antenna tuning solutions reported in the literature

Ref	Application area	Number of body positions considered	Frequency range, GHz	Measured minimum tuner loss, dB	Autonomous tuning (Y/N)	Integrated antenna (Y/N)
[39]	cellular	2	0.69–3.6	≃0.75	N	N
[12]	cellular	2	0.69–2.69	≃0.5	Y	N
[40]	cellular	2	0.85–1.95	0.3	N	N
this work	WSN	11	0.3–0.5	0.84	Y	Y

under Grant PC_2008_324. The authors thank Andrew Wallace of Applied Wave Research for their continued support with Microwave Office [26] and Oberdan Donadio and Dave Edgar for their support with ANSYS HFSS [42].

8 References

[1] Lymberis, A.: ‘Wearable smart systems: from technologies to integrated systems’. Annual Int. Conf. of the IEEE Engineering in Medicine and Biology Society, EMBC, 2011, 2011, pp. 3503–3506

[2] Gupta, N., Jilla, S.: ‘Digital fitness connector: smart wearable system’. First Int. Conf. on Informatics and Computational Intelligence (ICI), 2011, 2011, pp. 118–121

[3] Storni, C.: ‘Report on the reassembling health workshop: exploring the role of the internet of things’. J. Participants Medical Conf., 2010 Sep 27, vol. 2, p. e10

[4] Ali-Rantala, P., Sydanheimo, L., Keskilammi, M., *et al.*: ‘Indoor propagation comparison between 2.45 GHz and 433 MHz transmissions’. Antennas and Propagation Society International Symp., 2002, 2002, pp. 240–243, vol. **1**

[5] Weiss, M.D., Smith, J.L., Bach, J.: ‘RF coupling in a 433-MHz biotelemetry system for an artificial hip’, *IEEE Antennas Wirel. Propag. Lett.*, 2009, **8**, pp. 916–919

[6] Boyle, K.R.: ‘The performance of GSM 900 antennas in the presence of people and phantoms’. Twelfth Int. Conf. on Antennas and Propagation, 2003 (ICAP 2003), (Conf. Publ. No. 491), 2003, vol. **1**, pp. 35–38

[7] Morishita, H., Furuuchi, H., Fujimoto, K.: ‘Performance of balance-fed antenna system for handsets in the vicinity of a human head or hand’. IEE Proc. Microwaves, Antennas and Propagation, 2002, pp. 85–91

[8] Libelium: 'Wasp Mote platform', January 2015. Available at: http://www.libelium.com, Accessed May 2016
[9] Moog Crossbow: 'Mica 2 Mote', November 2015. Available at: http://www.moog-crossbow.com, Accessed May 2016
[10] Moog Crossbow: 'Mica dot Mote', November 2015. Available at: http://www.moog-crossbow.com, Accessed May 2016
[11] O'Flynn, B., Bellis, S., Delaney, K., *et al.*: 'The development of a novel miniaturized modular platform for wireless sensor networks'. Fourth Int. Symp. on Information Processing in Sensor Networks, 2005, IPSN 2005, 2005, pp. 370–375
[12] Boyle, K.R., Spits, E., de Jongh, M.A., *et al.*: 'A self-contained adaptive antenna tuner for mobile phones: featuring a self-learning calibration procedure'. Sixth European Conf. on Antennas and Propagation (EUCAP), 2012, 2012, pp. 1804–1808
[13] Qizheng, G., Morris, A.S.: 'A new method for matching network adaptive control', *IEEE Trans. Microw. Theory Techn.*, 2013, **61**, pp. 587–595
[14] Mukhopadhyay, S.C.: 'Wearable sensors for human activity monitoring: a review', *IEEE Sens. J.*, 2015, **15**, pp. 1321–1330
[15] Gemio, J., Parron, J., Soler, J.: 'Human body effects on implantable antennas for ISM bands applications: models comparison and propagation losses study', *Progr. Electromagn. Res.*, 2010, **110**, pp. 437–452
[16] Werber, D., Schwentner, A., Biebl, E.: 'Investigation of RF transmission properties of human tissues', *Adv. Radio Sci.*, 2006, **4**, pp. 357–360
[17] Ogawa, K., Matsuyoshi, T., Iwai, H., *et al.*: 'A high-precision real human phantom for EM evaluation of handheld terminals in a talk situation'. Antennas and Propagation Society Int. Symp., 2001, 2001, pp. 68–71
[18] Okoniewski, M., Stuchly, M.: 'A study of the handset antenna and human body interaction', *IEEE Trans. Microw. Theory Techn.*, 1996, **44**, pp. 1855–1864
[19] Buckley, J., McCarthy, K.G., O'Flynn, B., *et al.*: 'The detuning effects of a wrist-worn antenna and design of a custom antenna measurement system'. European Microwave Conf. (EuMC), 2010, 2010, pp. 1738–1741
[20] Buckley, J., O'Flynn, B., Haigh, P., *et al.*: 'Antenna tuning for wearable wireless sensors'. Sensors, 2011, 2011, pp. 1990–1993
[21] Buckley, J., Gaetano, D., McCarthy, K.G., *et al.*: 'Compact 433 MHz antenna for wireless smart system applications', *Electron. Lett.*, 2014, **50**, pp. 572–574
[22] Rohde & Schwarz: 'ZVRE 4 GHz, 2-port vector network analyzer', November 2015. Available at: https://www.rohde-schwarz.com, Accessed May 2016
[23] Loizou, L., Buckley, J., O'Flynn, B.: 'Design and analysis of a dual-band inverted-F antenna with orthogonal frequency-controlled radiation planes', *IEEE Trans. Antennas Propag.*, 2013, **61**, pp. 3946–3951
[24] Mathworks: 'Matlab 2011', September 2016. Available at: https://uk.mathworks.com, Accessed May 2016
[25] Yu-Shin, W., Ming-Chou, L., Shyh-Jong, C.: 'Two PIFA-related miniaturized dual-band antennas', *IEEE Trans. Antennas Propag.*, 2007, **55**, pp. 805–811
[26] A. W. R. (AWR): 'Microwave Office V.10', September 2016. Available at: http://www.awrcorp.com, Accessed May 2016
[27] Golio, M., Golio, J.: '*RF and microwave passive and active technologies*' (CRC Press, 2007)
[28] Pozar, D.M.: '*Microwave engineering*' (John Wiley & Sons, Inc., 2012, 4th edn.), p. 561
[29] Qizheng, G., De Luis, J.R., Morris, A.S., *et al.*: 'An analytical algorithm for Pi-network impedance tuners', *IEEE Trans. Circuits Syst. I, Regul. Pap.*, 2011, **58**, pp. 2894–2905
[30] Peregrine Semiconductor: 'PE64102, digital tunable capacitor', September 2016. Available at: http://www.psemi.com, Accessed May 2016
[31] Coilcraft: '0807SQ-14NJLB, air core inductor', January 2015. Available at: http://www.coilcraft.com, Accessed May 2016
[32] MiniCircuits: 'SYDC-20-62HP+ Coupler', September 2016. Available at: http://www.minicircuits.com, Accessed May 2016
[33] Keysight: 'Keysight (Agilent) ADS, 2011', Jaseptn 2016. Available at: http://www.keysight.com, Accessed May 2016
[34] Peregrine Semiconductor: 'PE4251, RF switch', September 2016. Available at: http://www.psemi.com, Accessed May 2016
[35] Linear Technology: 'LT5538, RF power detector', September 2016. Available at: http://www.linear.com, Accessed May 2016
[36] Atmega: 'AtMega128L, high-performance, 8-bit, RISC microcontroller', September 2016. Available at: http://www.atmel.com, Accessed May 2016
[37] Maury: 'Model 1878G triple-stub tuner (200 to 500 MHz)', September 2016. Available at: https://www.maurymw.com, Accessed May 2016
[38] Emerson & Cuming Microwave Products: 'ECCOSTOCK® PP-2, flexible, low loss, closed cell polyethylene foam', September 2016. Available at: http://www.lairdtech.com, Accessed May 2016
[39] Chen, Y., Martens, R., Valkonen, R., *et al.*: 'A varactor-based tunable matching network for a non-resonant mobile terminal antenna'. The 8th European Conf. on Antennas and Propagation (EuCAP 2014), 2014, pp. 1877–1881
[40] Sankey, L., Popovic, Z.: 'Adaptive tuning for handheld transmitters'. Microwave Symp. Digest, 2009, MTT'09, IEEE MTT-S Int., 2009, pp. 225–228
[41] Peregrine Semiconductor: 'UltraCMOS RFSOI', September 2016. Available at: http://www.psemi.com, Accessed September 2016
[42] ANSYS: 'High frequency structure simulator (HFSS) V14.0', September 2016. Available at: http://www.ansys.com, Accessed May 2016